frontiers | Frontiers in Materials

TYPE Original Research
PUBLISHED 10 July 2023
DOI 10.3389/fmats.2023.1190031

OPEN ACCESS

EDITED BY
Hui Yao,
Beijing University of Technology, China

REVIEWED BY
Haibo Ding,
Southwest Jiaotong University, China
Ali Raza,
University of Engineering and Technology, Taxila, Pakistan

*CORRESPONDENCE
Wenrui Yang,
wryang99@163.com

RECEIVED 20 March 2023
ACCEPTED 09 June 2023
PUBLISHED 10 July 2023

CITATION
Zhang K, Yang W, Tang Z, Wu W, Quan W and Wang S (2023), The effect of pore characteristics on the bonding properties of steam-cured concrete and GFRP bars. *Front. Mater.* 10:1190031.
doi: 10.3389/fmats.2023.1190031

The effect of pore characteristics on the bonding properties of steam-cured concrete and GFRP bars

Kai Zhang[1], Wenrui Yang[2]*, Zhiyi Tang[2], Weiwei Wu[3,4], Weijie Quan[2] and Shiyu Wang[2]

[1]Department of Road and Materials, Jiangxi Transportation Institute, Nanchang, China, [2]School of Civil and Architectural Engineering, East China University of Technology, Nanchang, China, [3]School of Transportation and Logistics Engineering, Wuhan University of Technology, Wuhan, China, [4]Hubei Province Highway Engineering Research Center, Wuhan, China

Steam cured concrete prefabricated components has the advantages of short construction period, less environmental pollution, convenient construction and low cost, and is widely used in high-speed railway projects. However, the changes of later strength, capillary water absorption and pore distribution led to the reduction of durability of steam-curing concrete and accelerated the damage speed of GFRP bars and bond performance between concrete and GFRP bars. In this study, the method of steam curing is adopted to simulate the damage of components caused by actual steam curing environment. The influence of pore characteristics on the bonding properties of steam cured concrete and GFRP steel bar is analyzed from both micro and macro perspectives. Analysis method combining pore characteristics with bonding strength. The test results showed that the hydration products of concrete were unaffected, but the density of the hydration products changed due to the steam curing. The porosity of the steam-cured concrete was much higher than that of the standard-cured concrete. The number of gel pores smaller than 20 nm accounted for 12.27% of the total number of pores on average, which was about twice the proportion of the gel pores of this size in the standard-cured concrete. The proportion of harmful voids with pore size of 50–200 nm and greater than 200 nm is higher than that of standard curing concrete. The bond strength of the steam-cured concrete and GFRP bars was 30% lower than that of the standard-cured concrete. With the change of the thickness of the concrete cover and the diameter of GFRP bars, the bond strength changed significantly. Based on the analysis of the test data, a predictive model of the bond strength deterioration for the steam-cured concrete and GFRP bars was established. The model fully accounted for influence factors such as the porosity, diameter, anchor length, and concrete strength.

KEYWORDS

steam-cured concrete, GFRP bars, bonding performance, pore characterization, damage prediction model

1 Introduction

In the process of general high-speed railway construction, the main load-bearing components such as track slab and prestressed simply-supported beams are mostly prefabricated components of steam-cured concrete. The steam curing method in high-speed railway essentially refers to adding water vapor during the curing process, which

accelerates the hydration rate of cement and the formation rate of concrete internal structure during the curing process, thus improving the early strength and hardening rate of concrete. Therefore, the use of steam curing concrete improves the production efficiency of concrete, to a certain extent, and reduces the construction time, and then produces greater economic benefits. At present, the application of autoclaved concrete prefabricated components has been put into use in many practical projects such as bridges and pavements and is gradually becoming mature.

According to statistics, it is a key issue that the service life of steam-curing precast concrete component greatly differs with the design life, which not only causes serious economic losses, but also cannot meet the requirements of high-speed railway construction for the safe development in China. The use of glass fiber reinforced plastic (GFRP) with strong corrosion resistance and high-cost performance ratio to replace or partially replace the steel bars in the steam curing concrete prefabricated components can effectively improve the corrosion of steel bars and increase the service life of concrete (Yang et al., 2017; Zhang et al., 2021). During the steam-curing process, a high-temperature and high-humidity environment accelerates the hydration reaction rate of concrete and has a certain impact on the concrete structure (Shi et al., 2021; Zhou et al., 2022). Jiang et al. (Jiang et al., 2017) and Shi et al. (Shi et al., 2020a) have proposed that the degree of hydration of the surface of steam-cured concrete is greater than that of the interior. The thermal gravimetric damage can reach 0.65%, which is twice as high as the value for standard-cured concrete, and the porosity and number of micro-cracks increase. Eventually, steam-cured concrete facilities deteriorate more quickly, which is one of the most significant challenges facing the international construction industry (Chen et al., 2019; Liu et al., 2019; Zou et al., 2019; Liu et al., 2020a; Yang et al., 2022).

Other researchers have improved the damage resistance and durability of precast concrete by changing the concrete composition, using additives and optimizing the steam curing system (Maruyama et al., 2017; Wang et al., 2022). Shi et al. (Shi et al., 2020b)showed that the thermal damage of steam-cured concrete will accelerate the corrosion of internal bars and reduce the bonding performance, leading to serious economic issues and safety hazards. However, there are few studies on the damage of bars in steam-cured concrete. Yang (Yang, 2016) proposed that the performance degradation of glass fiber reinforced plastic (GFRP) bars in steam cured concrete is far lower than that of ordinary steel bars, which effectively improves the durability and service life of steam cured components. Zeyad (Zeyad et al., 2021) found that adding fine palm oil waste ash to replace part of cement can reduce the damage to concrete caused by steam curing. Isleem (Isleem et al., 2021) conducted numerical and empirical research on the axial compression performance of GFRP reinforced concrete hollow columns using ABAQUS finite element software, and proposed a concrete damage plasticity model (CDPM) for complex column response. Furthermore, he proposed different empirical formulas and artificial neural network models for predicting the softening and hardening behavior of GFRP-RC concrete.

The bond performance between GFRP bars and concrete is one of the most important factors to evaluate the performance of GFRP reinforced concrete structures, and the sufficient bond performance is the basic requirement to ensure the cooperative work of reinforcement and concrete (Maranan et al., 2015; Yoo et al., 2015). Therefore, researchers have carried out most of the research on the bond performance between reinforcement and concrete, such as the type of reinforcement, the form of rib on the surface of reinforcement, the diameter of FRP reinforcement, and the thickness of concrete cover, which will affect the bond strength (Ellis et al., 2018; Wang et al., 2018; Wu et al., 2022). However, there are still insufficient researches on the influence of diameter of FRP bars, anchorage length and thickness of concrete protective layer on the bond performance of GFRP bars under steam curing environment, thus increasing the investment of steam-cured concrete in Engineering practice. However, in the steaming environment, the concrete will have the different degree of hydration reaction, also produce a large number of micro-pore and cause thermal damage to various materials in the concrete, which will affect the bonding performance between GFRP bars and concrete (Han et al., 2019; Bi et al., 2021; Zou et al., 2021). The porosity of concrete directly affects the bond area between GFRP bars and steam cured concrete, which leads to the decrease of bond performance. However, there have been few studies on the effect of the pore characteristics on the bonding properties of steam-cured concrete.

The existing research only discusses the mechanical properties, time cost, early strength, convenience and practicality of steam cured concrete, but ignores the influence of structural stability and structural distribution on the performance of steam cured concrete in the middle term. Due to the influence of steam curing on the internal pore characteristics of concrete, a brief introduction will be given to the related properties of concrete. So, in this paper, the influence of pore characteristics of steam cured concrete on the bond performance is studied from the micro and macro perspectives, and the bond mechanism between steam cured concrete and GFRP reinforcement is revealed from the perspective of pore size distribution. Furthermore, the influence was quantified, and a model was established to predict the relationship between the porosity and the bonding performance. This provides a theoretical

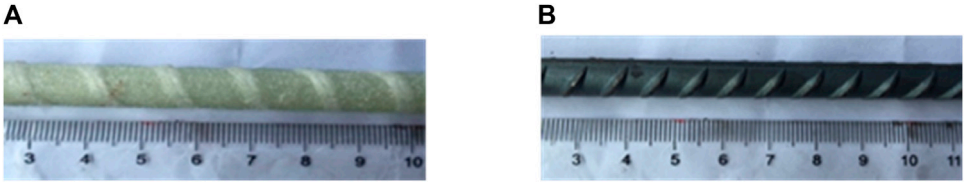

FIGURE 1
GFRP bar **(A)** and steel bar **(B)**.

10.3389/fmats.2023.1190031

TABLE 1 Tensile test results of GFRP bars.

Temperature	Relative humidity	Extensometer gauge length	Diameter	Ultimate tension	Tensile strength	Elasticity modulus
˚C	%	mm	*d*/mm	F/kN	R/MPa	E/MPa
20	40	100	10	88	1,023	51,900
				95	1,107	51,800
				93	1,089	51,000
				97	1,131	51,700
Mean value				92	1,087	51,600
20	40	100	16	85	932	47,000
				92	921	47,300
				86	917	47,200
				89	910	47,300
Mean value				88	920	47,200
20	40	100	19	85	871	46,500
				81	875	47,200
				82	885	46,800
				84	897	47,500
Mean value				83	882	47,000
20	40	100	22	78	724	46,600
				79	735	46,000
				82	732	46,200
				77	729	46,800
Mean value				79	730	46,400

TABLE 2 GFRP bars/reinforced steam-cured concrete beams.

Maintenance method	Reinforcement type	Diameter: *d*	Concrete beam: *b*×*h*×*L*	Concrete cover thickness	Beam number	Working condition abbreviation
		(mm)	(mm)	*c* (mm)		
Steam curing	GFRP bars	10	80 × 110×1,100	15	1–4#	G-Ste1-1
		10	80 × 110×1,100	20	5–8#	G-Ste1-2
		10	80 × 110×1,100	25	9–12#	G-Ste1-3
		10	80 × 110×1,100	35	13–16#	G-Ste1-4
		16	150 × 150×1,100	25	17–20#	G-Ste2
		19	178 × 178×1,100	25	21–24#	G-Ste3
		22	206 × 206×1,100	25	25–28#	G-Ste4
	Steel bars	10	80 × 110×110	25	29–32#	S-Ste
Standard Conservation	GFRP bars	10	80 × 110×110	25	33–36#	G-Sta

basis for the modification of the concrete performance parameters for the design of steam-cured GFRP-reinforced concrete precast members.

2 Test

2.1 Experiment material

(1) GFRP and steel bars A comparison test was carried out using steel bars with diameters of 10 mm.

The GFRP bars have a helical indent formed by wrapping a resin-impregnated E-glass tow along the length of the bar with a pitch, L, of 14 mm and a depth, h, of 0.325 mm (Figure 1). The designated diameters are 10, 16, 19, and 22 mm, respectively. The equivalent diameters of the bars, d, measured by the writers using the immersion method, are 10.2, 16.3, 19.1, and 22.2 mm (immersed cross-sectional areas = 82, 209, 286 and 387 mm^2). The relevant mechanical parameters provided by the tensile test are shown in Table 1. The tensile tests of GFRP bars were performed by an SHT4106-G type microcomputer control electro-hydraulic servo universal testing machine (ACI American Concrete Institute, 2005). Loading force was recorded by the automatic sensor. To prevent shear failure on both ends of the GFRP bars, a 250-mm-long steel pipe anchorage was fixed on the GFRP bar ends.

(2) Concrete

The concrete was provided by a local ready-mix plant and had a water-to-cement ratio of 0.59. The coarse aggregate shall be 5–20 mm continuously graded natural aggregate with crushing index of 12% and bulk density of 1,400–1700 kg/m^3. The sand had medium coarseness with a fineness modulus of 2.8. The cementitious material consisted of 75% by weight of Type I Portland cement with pH 12.65% and 25% Class F fly ash. The tensile strengths of the standard-cured and steam-cured concrete were measured to be 3.14 and 2.93 MPa, respectively.

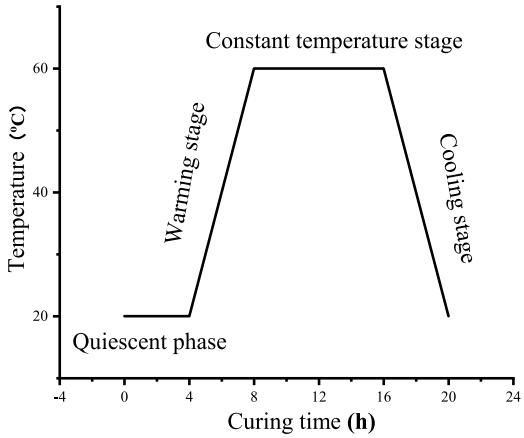

FIGURE 2
Steam curing method.

2.2 Sample fabrication

(1) GFRP bars/reinforced concrete prisms

There was some variability in the porosity due to the different amounts of damage to the surfaces and interiors of the concrete caused by the steam curing. Therefore, in this test, the concrete-prism with 10 mm GFRP reinforcement and 15mm, 20mm, 25mm and 35 mm thickness of concrete cover was used for microstructure observation and pore structure test. After 28 days of curing, cut the concrete with German automatic cutting-machine, and then dry the bonding section for microstructure observation and pore structure test.

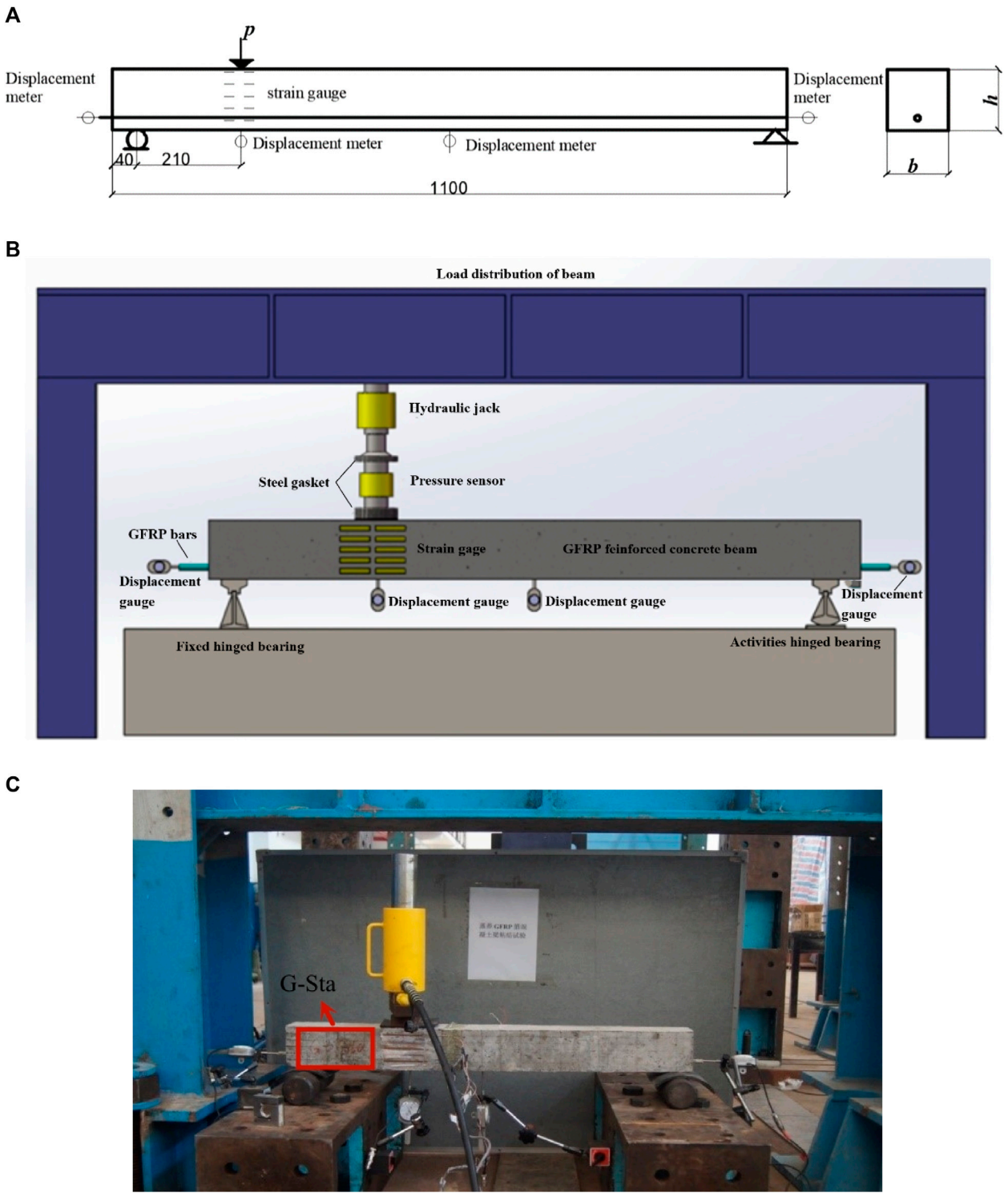

FIGURE 3
Three-point beam bonding test: **(A)** Test schematic (unit: mm); **(B)** Test model diagram; and **(C)** Field test pictures.

(2) GFRP bars/reinforced concrete beams

Esfahani et al. (Esfahani et al., 2013) compared the test data and calculation results of GFRP reinforced concrete beams (ACI American Concrete Institute, 2006). The comparison showed that the evaluation of the bond performances of the GFRP bars and concrete without lateral reinforcement was not conservative enough and even overestimated. Therefore, it is important to study the bonding between GFRP bars and concrete without lateral reinforcement. In order to avoid the influence of transverse

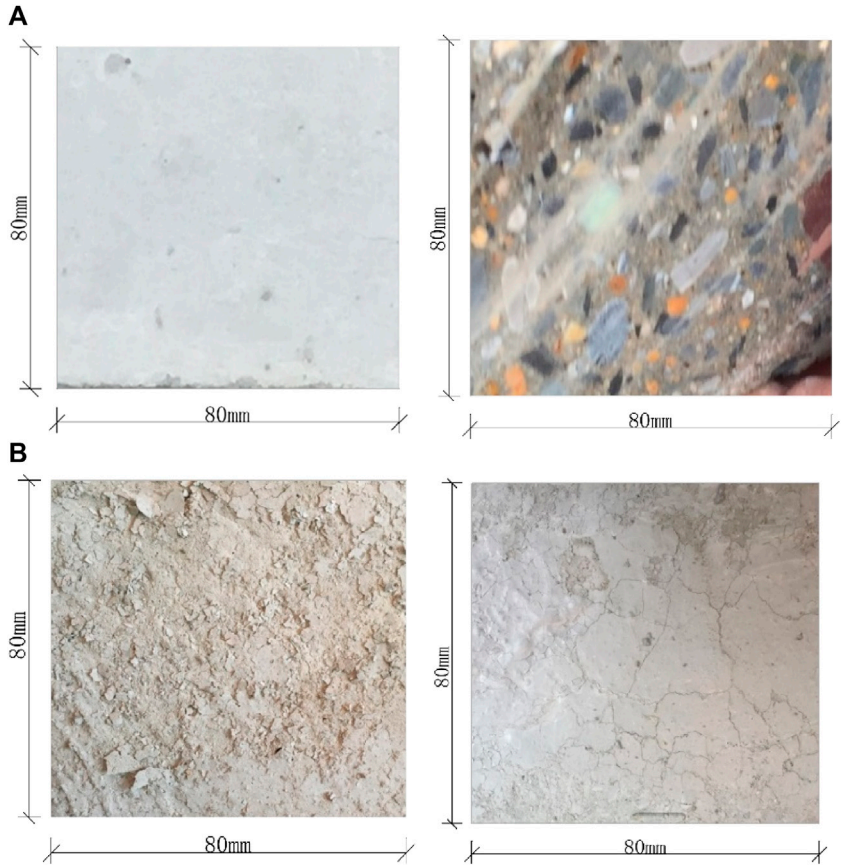

FIGURE 4
Concrete surface morphology diagram: **(A)** Standard curing concrete specimens and Steam cured concrete cutting surface; **(B)** Steam cured concrete surface.

reinforcement and other factors on the bond performance, this paper only installs a tensile GFRP bar at the bottom of the beam.

In this study, steam-cured reinforced concrete beams were used as comparison specimens. The variables set in the test are: curing method, reinforcement diameter and cover thickness. Three-point beam bond tests were conducted on the corresponding GFRP reinforced concrete beams. The thermal damage behaviors of the steam-cured GFRP-reinforced concrete beams were studied. Four test beams were prepared for each group. All the abbreviations for the beam conditions are shown in Table 2.

2.3 Curing condition

Two curing methods, standard curing and steam curing, were used to compare and analyze the influence of different maintenance processes on bonding performance.

(1) Standard curing method:

After pouring the standard-cured specimens, specimens were kept at 20°C ± 5°C for 1–2 days, then they were kept in a standard curing room at 20°C ± 2°C and 95% relative humidity for curing 28 days after the molds were removed.

(2) Steam curing method:

The purpose of steam curing concrete is to accelerate the hydration rate of cement under the action of a moist heat medium (water vapor), which accelerates the rapid formation of the internal structure of the concrete and promotes early strength and fast hardening. However, different steam curing methods will cause different physical, chemical, and mechanical changes in the concrete, which lead to different types of thermal damage during the steam curing process (Liu et al., 2020b; Wang et al., 2020). At present, the curing regime refer to *TZ 210–2005* (Wikidata, 2005). In this research, the quiescent phase was determined to be 4 h at normal temperature, 4 h for heating, 8 h at 60°C ± 5°C, and 4 h for cooling according to the construction quality acceptance standards for high-speed railway bridges and culverts (Figure 2). According to the humidity and temperature conditions in Wuhan, China, the number of steaming days is set at 14 days.

2.4 Test method

(1) Microscopic observations

Microscopic observations of the microstructure of steam-cured concrete were performed via scanning electron microscopy. The cut

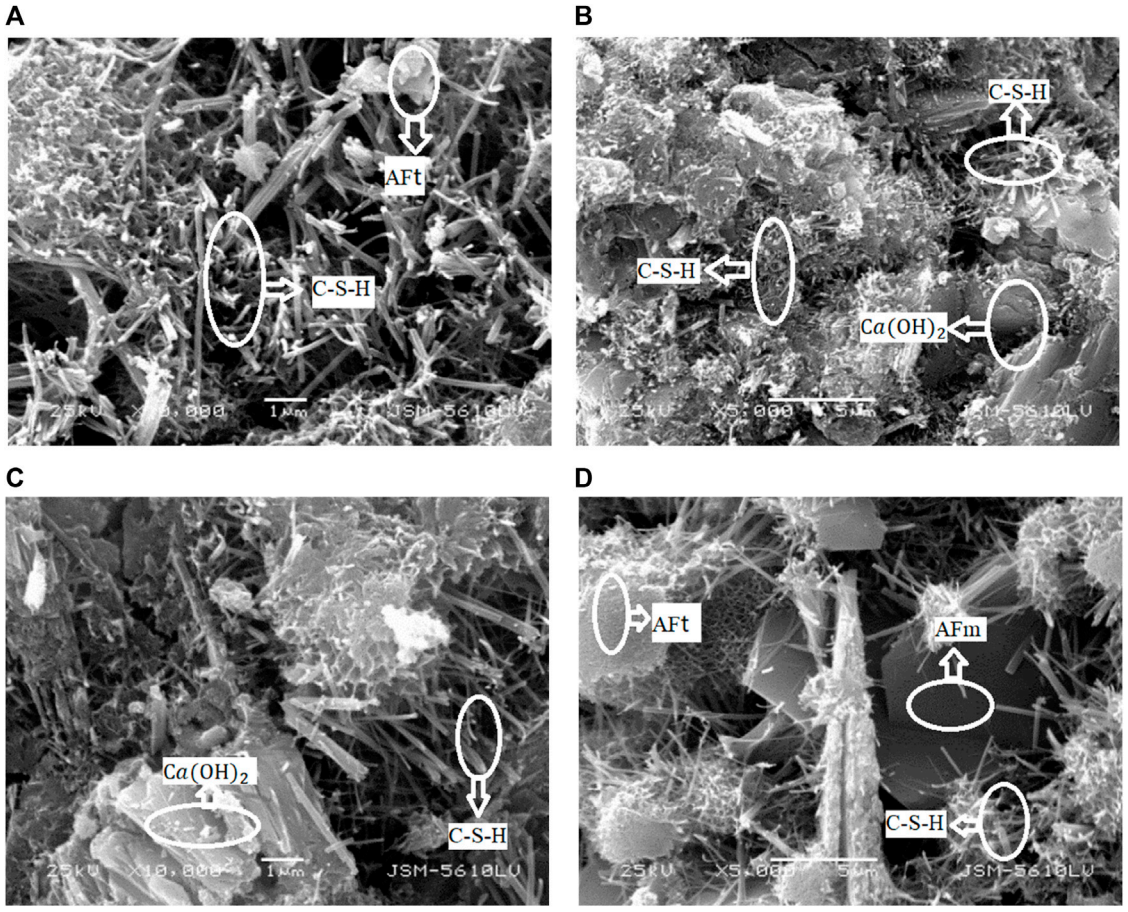

FIGURE 5
SEM figures of hydration products and their distribution of concrete with different curing methods: **(A)** Standard curing concrete surface (× 10,000); **(B)** Standard curing concrete surface (× 5,000); **(C)** Steam curing concrete (× 10,000); and **(D)** Steam curing concrete (× 5,000).

section of steam cured concrete is observed, and the microstructure characteristics of steam cured concrete under different conditions are analyzed. According to the theory of composite materials, the micro mechanism of thermal damage of steam cured concrete is analyzed.

(2) Pore structure distribution

The research emphasis on the internal structure of concrete materials has shifted to the testing and evaluation of pore gradation, pore morphology and porosity. In this paper, the pore structure distribution in the bonding surface of steam cured, and standard cured concrete was studied by mercury intrusion test. The mercury intrusion test is based on the functional relationship between the pressure applied to cement-based or other porous material systems, and the amount of mercury injected (Cieszko et al., 2019; Sidiq et al., 2020). The pore volume and the pore size were calculated. In this study, the pore size distribution of concrete samples after 28 days of steam curing and standard curing was quantitatively analyzed. First, dry the sample, then cut it into 5–7 mm concrete particles and immerse it in anhydrous ethanol for 3–4 days to stop hydration. Finally, the sample is dried in a drying oven until the sample has a constant weight, and the pore structure is determined by applying pressure in the mercury test.

(3) Three-point beam test method

The test method for assessing the bonding performances of the GFRP bars with concrete included an articulated beam bending test and a pulling test based on pulling in a well-anchored concrete block or column (Al-Sibahy and Sabhan, 2020; Esmaeili et al., 2020; Rossi et al., 2020). Zheng et al. (Zheng et al., 2016) conducted a comparative study based on beam and pull-out tests. They found that the bond strengths determined via the hinged beam test were significantly less than those of the pull-out test due to fewer bond constraints and more longitudinal cracks. Bakis et al. (Bakis et al., 2007) also suggested that the bond strengths measured by the three-point eccentric load beam test were different from those obtained by the pull-out test. This difference is mainly because the beam bond performance test considers the existing shear or bending moment of the actual member.

The three-point eccentric-load bonding performance tests of the GFRP-reinforced concrete beams were carried out using a reaction frame and a hydraulic jacking device. Based on the results of the three-point bending optimal anchorage length test in the previous study (Sidiq et al., 2019), the test used 250 mm anchorage section and load application location 210 mm from the support. A schematic diagram of the test device layout is shown in Figure 3,

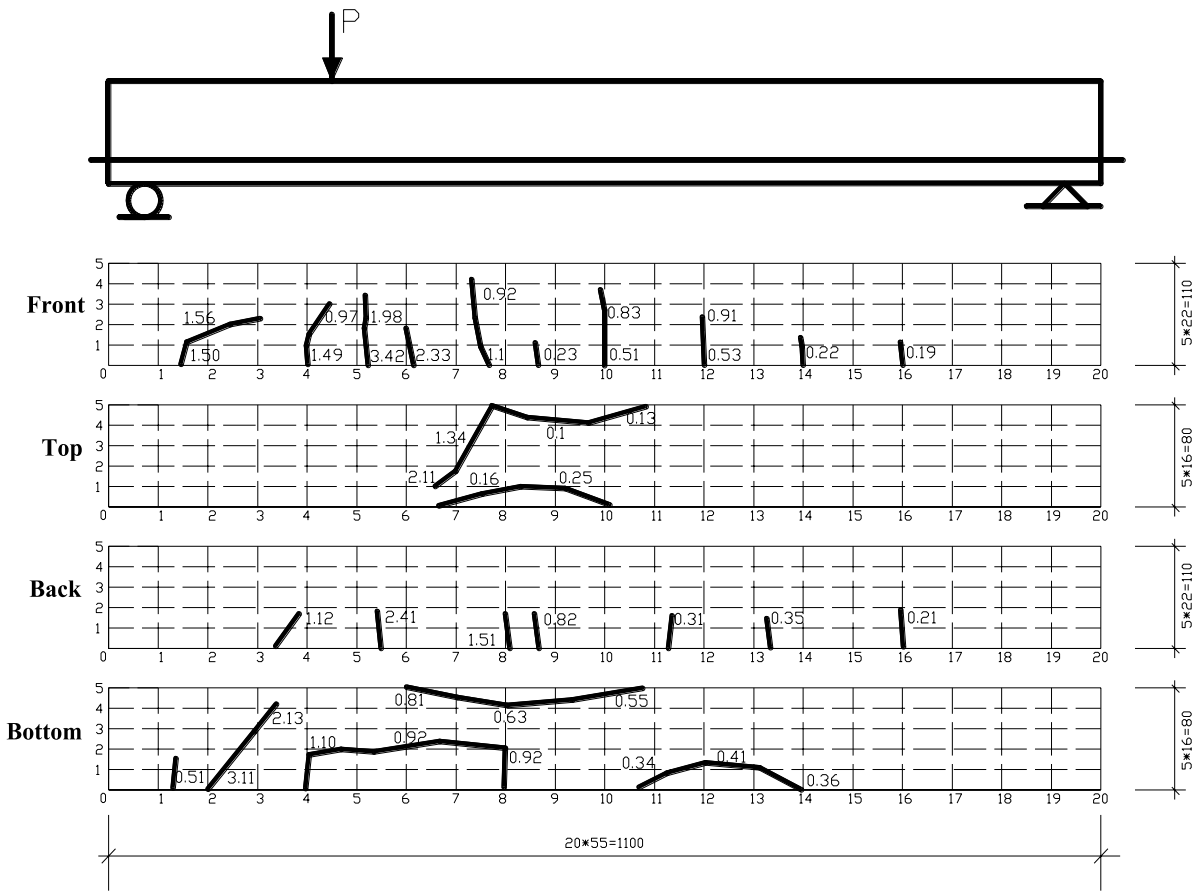

FIGURE 6
G-sta beam crack development diagram: the number next to the crack is the cracking load, kN. (unit: mm).

along with the field test images. The load slip curve and crack development shall be recorded during the test. According to the test data, sliding load and maximum bond strength theory, the bond properties of autoclaved concrete and reinforcement under different conditions are compared and analyzed. The deterioration of the bonding performances for the steam-cured concrete and GFRP bars were determined.

3 Analysis of test results

3.1 Apparent appearance of steam-cured concrete

A comparison of Figures 4A, B shows that the surface of the steam-cured concrete produced clear peeling and micro-cracks, whereas the surface of the standard-cured concrete was relatively smooth. However, after cutting and polishing, the concrete cutting surface showed aggregated particles with different sizes and shapes and discontinuous cement paste. Therefore, the apparent morphology of the steam-cured concrete showed that the steam curing caused thermal damage to the concrete surface, but the steam-cured concrete was still a two-phase material with aggregate particles dispersed throughout the cement slurry matrix, which was no different from the standard-curing concrete.

3.2 Hydration product micromorphology

The microstructure of steam cured concrete is very important to study its performance mechanism. The composition of concrete will change the hydration products of cement, and different curing environment and curing age will also have a certain impact on the degree of cement hydration. Therefore, it is necessary to consider the influence of concrete composition, curing environment, curing age and other factors on the microstructure. As the transition zone between concrete grout and interface will change with the change of ambient temperature, humidity and time, the microstructure of concrete is not inherent to the material. During steam curing, the degree of hydration of cement may be affected due to the difference in temperature and humidity between the surface and the middle of concrete in direct contact with the bottom surface. Therefore, this paper makes a comparative analysis between standard curing concrete and steam curing concrete.

TABLE 3 Pore structure distribution of concrete.

Maintenance method	Specimen number	Porosity	Solid-pore ratio	Pore size distribution			
				(%)			
				<20	20–50	50–200 nm	>200 nm
		(%)	(%)	nm	nm		
Steam curing	G-Ste1-1	13	86	13	55	17	15
	G-Ste1-2	14	86	12	54	17	17
	G-Ste1-3	13	87	12	54	16	18
	G-Ste1-4	12	88	11	54	17	18
	mean	13	86.7	12	54.3	16.8	17
	Standard deviation	0.7	0.8	0.7	0.4	0.4	1.2
	Coefficient of variation	5.3	0.9	5.8	0.7	2.3	7
Standard maintenance	G-Ste1-1	8	92	6	67	15	12
	G-Ste1-2	7	93	7	65	16	13
	G-Ste1-3	7	93	7	68	15	11
	G-Ste1-4	6	94	6	63	16	15
	mean	7	93	6.5	65.7	15.5	12.7
	Standard deviation	0.7	0.7	0.5	1.9	0.5	1.5
	Coefficient of variation	10	0.8	7.7	2.9	3.2	11.8

Figure 5 shows the microstructure of standard curing and steam curing concrete. The scanning electron microscopy images of the microstructure of the concrete at a 10,000× resolution showed needle-like crystals of calcium sulfur aluminate hydrides (ettringite), which appeared mainly due to the reaction of calcium, sulfate, aluminate, and hydroxide in the early stage of hydration. With the progress of hydration, prismatic calcium hydroxide crystals and fibrous calcium silicate flocs continue to fill between the undissolved cement particles. The "calcium alumina" may have decomposed into hexagonal flakes of mono-sulfurous sulfur aluminate hydrates. Figure 6 shows that at 10,000 × There is obvious acicular crystal hydrate at the resolution of 5,000 × A columnar calcium hydroxide crystal is observed at resolution. The comparative analysis of the microstructure and morphology of standard curing concrete and steam curing concrete shows that the surface hydration degree of the latter is significant and the hydration crystal is dense. This shows that steam curing accelerates the hydration degree of concrete and affects the overall density, making the porosity and cracks of steam curing concrete more obvious. This is also related to the formation of water loss products during the hydration reaction process.

3.3 Pore structure of steam-cured concrete

The pore structures inside the concrete had different sizes and shapes, which directly affected the material properties of the concrete. The strength and permeability of concrete have an exponential relationship with the porosity, and the porosity of concrete directly determines the bonding area with the internal bars. Therefore, the porosity was one of the decisive factors of the macroscopic mechanical properties and durability of the concrete.

3.3.1 Analysis of test results of concrete pore structure

The pore-gradation, porosity and morphology characterization of concrete have become the research focus of concrete materials. Sidiq et al. (Sidiq et al., 2020) (Sidiq et al., 2019) divided the pore-size of cement-based image materials into the gel pores (pore size is less than 10 nm); capillary pores (pore size is 5–5,000 nm), large pores (air formation) and insufficient pores. In this study, based on the appearance shown in Figure 6, the curing method of high-temperature and high-humidity has caused some damage to the concrete surface, making its surface pores and cracks more obvious. Table 3 shows that the porosity of steam curing concrete is significantly higher than that of standard-curing concrete, while the corresponding solid hole ratio is lower than that of standard curing concrete. The number of gel pores smaller than 20 nm accounted for 12.27% of the total number of pores, which was about twice the proportion of these gel-pores in the standard-cured concrete. This is mainly because the high-temperature steam environment accelerates the hydration reaction of cement clinker, promotes the formation of gel, such as

10.3389/fmats.2023.1190031

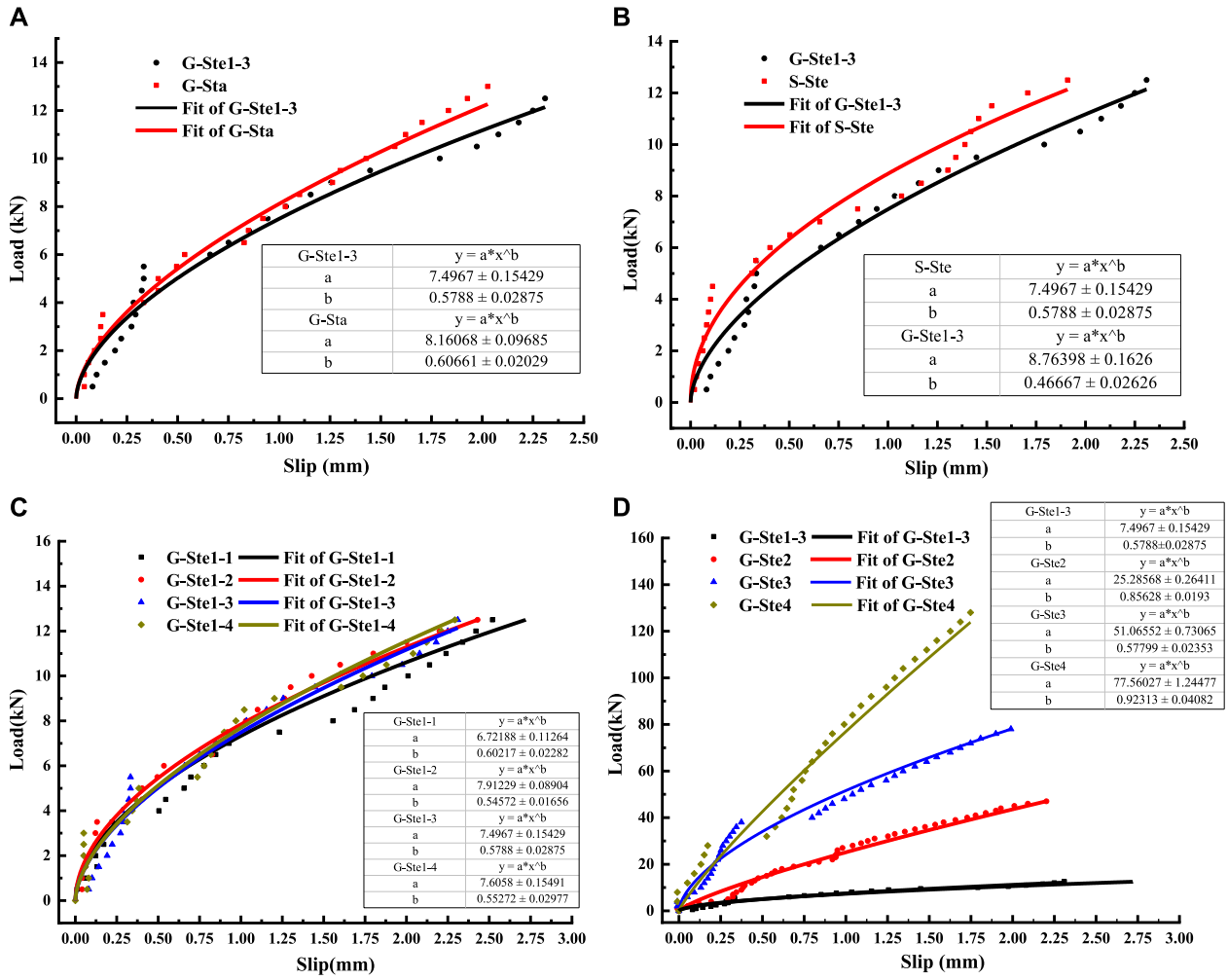

FIGURE 7
Load-slip curve: **(A)** Different maintenance methods; **(B)** Different bars; **(C)** Different concrete cover thickness; and **(D)** Different GFRP rib diameter.

hydrated calcium silicate and calcium aluminate, and ultimately leads to a large increase in the number of gel pores.

The apertures could be divided into harmless pores (apertures less than 20 nm), less harmful pores (apertures of 20–50 nm), harmful pores (apertures of 50–200 nm), and more harmful pores (apertures larger than 200 nm). Some studies have shown that pore diameters less than 50 nm have no effect on the performance of concrete and even can improve the performance (Hong et al., 2018; Qiu et al., 2019). However, pore diameters greater than 100 nm have a greater adverse effect on the performance of concrete. Table 3 shows that the lower hazard classes (pore sizes of 20–50 nm) in steam-cured concrete have a lower proportion of total pore size than standard-cured concrete, while the higher hazard classes (pore sizes greater than 50 nm) have a higher proportion of total pore size than standard-cured concrete. The detrimental porosity of concrete cured with steam was 33.8%, which was 5.9% greater than that of conventionally cured concrete. This implies that the distribution of pores over inside steam-cured concrete produces higher damage to the concrete structure, which not only affects the bonding area of the GFRP bars to the concrete but also their bonding characteristics. This is also the primary reason why chloride ion penetration is less than that of conventionally cured concrete.

3.4 Analysis of changes in bonding performance between concrete and GFRP

In the three-point beam bond test, most of the members show shear failure, and the initial cracks appear near the load application point. As the load was continuously applied, the edge cracks continued to increase until the main cracks appeared (Figure 6).

3.4.1 Load–slip curve

Figure 7A shows that, compared with the GFRP reinforced concrete beams under standard curing, the beam members under steam curing have 1.34 times of slip, and the ultimate load has decreased by 4%. The steam curing system had a certain degradation effect on the bonding performance of the GFRP bars and concrete. Figure 7B shows that the slippage of steam cured GFRP reinforced concrete beams is 1.42 times that of ordinary steam cured beam

10.3389/fmats.2023.1190031

TABLE 4 Bond slip parameters of steam-cured GFRP reinforced concrete beam.

Contrast	Specimen number	Maximum slip	Slip parameter	Slip parameter	Slip load	Maximum bond strength
		S_{max}: (mm)	a	C	N_{smax} :(kN)	τ_{max} :(MPa)
Different forms of maintenance	G-Sta	2	0.58	4.3	27	2.3
	G-Ste1-3	2.3	0.57	3.3	26	1.9
Different bars	S-Ste	1.9	0.48	1.2	27	0.6
	G-Ste1-3	2.3	0.58	3.3	26	1.9
Different concrete cover thickness	G-Ste1-1	2.5	0.67	2.3	23	1.4
	G-Ste1-2	2.4	0.52	2.7	25	1.6
	G-Ste1-3	2.3	0.58	3.3	27	1.9
	G-Ste1-4	2.3	0.58	4.5	31	2.6
Different diameters	G-Ste1-3	2.3	0.58	3.3	27	1.9
	G-Ste2	2	0.8	6.2	67	3.4
	G-Ste3	2	0.6	7.7	91	4
	G-Ste4	1.8	0.85	12	121	5.4

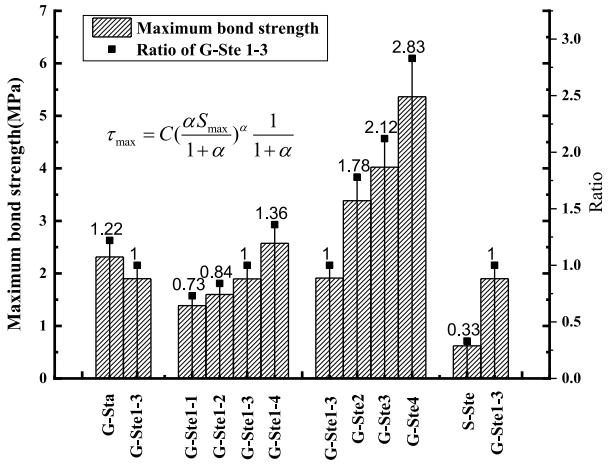

FIGURE 8
GFRP reinforced concrete beam maximum bond strength.

members. Figure 7C shows that under different concrete cover thickness conditions, the bonding properties of the GFRP bars and the steam-cured concrete did not show significant changes. Figure 7D shows that the variation rate of the bond–slip curve was the fastest when the diameter was 10 mm, and the curve variation rate was the lowest when the diameter was 19 mm.

3.4.2 Maximum bond strength

The traditional average bond strength ignores the amount of slipping or cracking change between the components during the stress process. If the sliding load and stress per unit area of the two materials are the same, the bond strength is also the same. The maximum bond strength theory used in this study is based on experiments and calculations of material mechanics. The theory relates the actual material slip relationship and the material properties, so it is better for use in analyzing the bond strengths between steam-cured concrete and different reinforcements. The variation of the bond strength between the steam-cured concrete and the GFRP bars can be explained by the degree of damage.

The bond–slip mechanism of the steam-cured concrete and the GFRP bars was similar to that of the standard-cured concrete. Therefore, the bond–slip constitutive relationship also conformed to the modified Bertero-Popov-Eligehausen (mBPE) bond–slip constitutive relationship. As the steam curing caused some damage to the bonding performance of the two, the steam-cured concrete and the GFRP bar were analyzed based on the theoretical maximum bonding strength using the typical mBPE bond–slip constitutive model and the test data of the bar bonding performance deterioration, as described in this section.

The mBPE model is mainly used to analyze the bond–slip relationship for the fiber-reinforced plastic (FRP) and concrete. This model was obtained by the modification of the Bertero-Popov-Eligehausen (BPE) bond–slip constitutive model (Zou et al., 2021) (Cosenza et al., 1995; Altalmas et al., 2015; Yan and Lin, 2017). The horizontal section with a constant bond strength is not considered in the mBPE model. The expression is as follows:

$$\frac{\tau}{\tau_{max}} = \begin{cases} \left(\frac{s}{s_{max}}\right)^{\alpha} & (0 < s < s_{max}) \\ 1 - \rho\left(\frac{s}{s_{max}} - 1\right) & (s_{max} < s < s_c) \\ \frac{\tau_c}{\tau_{max}} & (s < s_c) \end{cases} \quad (1)$$

where τ is the bond strength. τ_{max} is the maximum bond strength. τ_c is the corresponding bond strength at the beginning of linear slip.S is the slip value. s_{max} is the corresponding slip value τ_{max}. s_c is the

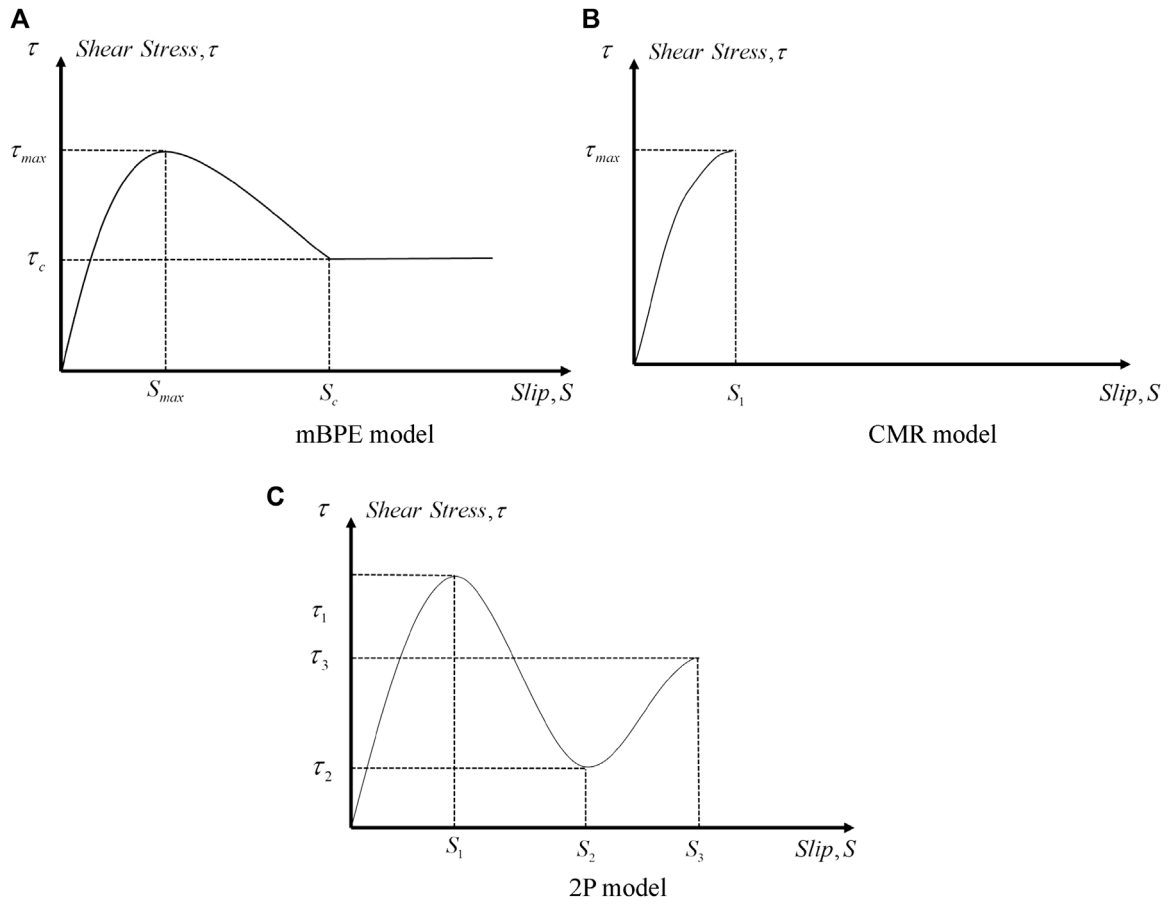

FIGURE 9
Bond slip model. **(A)** mBPE model **(B)** CMR model **(C)** 2P model.

corresponding slip value τ_c . α and ρ are the fitting parameters of the test data.

To further improve the accuracy of the mBPE model in analyzing the bond slip of FRP-reinforced concrete structures, Bakis et al. (Bakis et al., 2007) and Focacci et al. (Focacci et al., 2000) modified the mBPE model and proposed the expressions shown in Equations 2, 3. The curve produced by the modified mBPE model mainly intersects the curve in Figure 9 with the abscissa axis. The third stage with a constant slip strength can be simplified into a graph closed with the transverse coordinate axis. The expressions of the maximum bond slip load and maximum bond strength are shown in Equations 4, 5. The Levenberg Marquardt theory is used to determine the unknown parameters through the square difference between the test slip load and the theoretical slip load of GFRP bars (Bakis et al., 2007) (Press et al., 2007; Troian-Gautier et al., 2016; Xu et al., 2017).The calculation results of each specimen are shown in Table 4.

$$\tau = CS^{\alpha}\left(1 - \frac{S}{\bar{S}}\right) \tag{2}$$

$$S_{\max} = \alpha\bar{S}\Big/(1+\alpha) \tag{3}$$

$$N_f = S^{(1+\alpha)/2} \cdot \sqrt{4CE_f A_f \pi d_b \Big/ (1+\alpha)(2+\alpha)} \tag{4}$$

$$\tau_{\max} = C\left(\frac{\alpha\bar{S}}{1+\alpha}\right)^{\alpha}\frac{1}{1+\alpha} \tag{5}$$

Bakis et al. (Bakis et al., 2007)obtained the following expressions for the local maximum bond strength ($\tau_{\max}$) and the maximum slip load (N_{smax}) based on the mBPE model:

$$\tau_{\max} = C\left(\frac{aS_{\max}}{1+a}\right)^{a}\frac{1}{1+a} \tag{6}$$

$$N_{\mathrm{smax}} = \sqrt{4\pi d A_b E_b}\sqrt{c\Big/(1+a)(2+a)}s^{(1+a)/2} \tag{7}$$

As shown in Table 4 and Figure 8, the bonding strengths of the GFRP bars reached three times that of the steel bars. In addition, due to the corrosion resistance of the two reinforcement materials, the bond performance of ordinary reinforcement and GFRP reinforcement will be different. Therefore, the method of using the GFRP bars to replace or partially replace steel bars in steam-cured concrete components is worth popularizing and has certain engineering significance.

The maximum bond strength of GFRP reinforced concrete was reduced from 2.31 MPa to 1.90 MPa, and the reduction range

10.3389/fmats.2023.1190031

TABLE 5 RMSE of the mBPE, 2P and CMR models.

Specimen		RMSE		
		mBPE	CMR	2P
Different forms of maintenance	G-Sta	0.0582	0.0938	0.0395
	G-Ste1-3	0.0255	0.0343	0.0174
Different bars	S-Ste	0.0072	0.0075	0.0072
	G-Ste1-3	0.0255	0.0343	0.0174
Different concrete cover thickness	G-Ste1-1	0.0262	0.0396	0.016
	G-Ste1-2	0.0188	0.0215	0.0172
	G-Ste1-3	0.0255	0.0343	0.0174
	G-Ste1-4	0.0331	0.0469	0.0252
Different diameters	G-Ste1-3	0.0255	0.0343	0.0174
	G-Ste2	0.0246	0.0337	0.0147
	G-Ste3	0.0389	0.039	0.0386
	G-Ste4	0.0538	0.0923	0.0401

after steam curing was 22%.Wang (Wang, 2013) proposed that the reduction factor K_T of the bond strength between the GFRP bars and the concrete was 0.8 when the temperature was lower than 200°C, and K_T was taken as 0.65 when the temperature was between 200°C and 300°C. The reduction ratio of the bonding strength of the concrete and the GFRP bars was relatively large after steam curing at high temperatures, which showed that steam curing did indeed diminish the bond performance of the concrete and the GFRP bars. The decrease of bond performance is closely related to the change of structural performance of concrete during hydration and after high temperature steam curing.

The maximum bond strength of GFRP reinforced concrete after steam curing increases with the increase of concrete cover thickness. When the thickness of the concrete cover was in the range of 15–20 mm, the maximum bonding strength increased by 15%. When the thickness of the concrete cover was in the range of 20–25 mm, the maximum bonding strength increased by 19%. When the thickness of the concrete cover was in the range of 25–35 mm, the maximum bond strength increased by 35%. This is mainly related to the structural performance of steam cured concrete, and more cracks and pores on its surface layer are shown in Figure 4. These would provide more channels for external media to enter the interior of the concrete, affecting the internal reinforcement and the bonding interface. Therefore, the damage in steam cured concrete is relatively small. When the thickness of concrete cover is 35mm, the bonding performance is significantly enhanced.

Figure 8 shows that the maximum bond strength of steam cured concrete and GFRP reinforcement increases with the increase of diameter. When the diameter was in the range of 10–16 mm, the bond strength increased by 78%, which was not only related to the steam curing damage but also had a significant relationship with the ratio of C/d_b to d_b/l_e.

3.4.3 Theoretical analysis

The bond-slip constitutive model proposed by early researchers provides an effective method to study the bond-slip behavior between FRP bars and concrete. However, the single model cannot satisfy most of the studies for different test and engineering applications. Based on this, researchers modified the bond-slip model of foundation to obtain a more applicable bond-slip constitutive model. At present, the existing bond slip models mainly include the Malvar, the Bertero-Eligehausen-Popov (BPE), the modified BPE (mBPE), the Cosenza-Manfredi-Realfonzo (CMR), the Wei (2P),etc. As shown in Figure 9, the main test process in the bond-slip test is located in the ascending section on the bond-slip curve. When the test is in the pull-out stage of the FRP bar, the mBPE curve appears as a curve downtrend until it maintains a horizontal straight line in the final stage. The CMR model can only describe the ascending segment of the bond-slip curve, and lacks the curve expressing the decreasing segment and the horizontal segment of the bond strength, which is more in line with the trend of the experimental data from this paper. The 2P theoretical model is based on the establishment of the bond-slip curve, which can more accurately express the changing trend of the curve. The expression of the mBPE model is shown in Eq. 1.

3.4.3.1 CMR model

In order to solve the problem that Malvar model did not conform with the test results because of its complex formula, unclear physical meaning of parameters and small initial slope to

10.3389/fmats.2023.1190031

TABLE 6 The parameters of the mBPE, CMR and 2P models.

Specimen		mBPE		CMR			2P					
		τ_{max} (MPa)	a	τ_{max} (MPa)	β	S_r	τ_{max} (MPa)	b	η	ω	φ	c
Different forms of maintenance	G-Sta	2.3100	0.5840	2.5600	0.7881	1.2544	2.2514	−2.9576	0.7120	−0.0003	0.4069	2.8930
	G-Stel-3	1.9000	0.5770	2.1000	0.7865	1.3707	1.8701	−2.3978	0.6143	−0.0004	0.3679	2.4116
Different bars	S-Ste	0.6200	0.4850	0.7000	0.5906	1.4297	0.5923	−1.3795	1.1199	−0.0003	1.1254	0.6624
	G-Stel-3	1.9000	0.5770	2.1000	0.7865	1.3707	1.8701	−2.3978	0.6143	−0.0004	0.3679	2.4116
Different concrete cover thickness	G-Stel-1	1.3800	0.6650	1.5000	1.0059	1.3028	1.3536	−2.0281	0.4569	−0.0003	0.3801	1.9493
	G-Stel-2	1.6100	0.5250	1.8500	0.6518	1.8570	1.5545	−2.1185	0.7378	0.0002	−0.6555	1.8342
	G-Stel-3	1.9000	0.5770	2.1000	0.7865	1.3707	1.8701	−2.3978	0.6143	−0.0004	0.3679	2.4116
	G-Stel-4	2.5700	0.5860	2.9000	0.8022	1.4462	2.5223	−4.0255	0.6301	−0.0001	0.7057	3.2448
Different diameters	G-Stel-3	1.9000	0.5770	2.1000	0.7865	1.3707	1.8701	−2.3978	0.6143	−0.0004	0.3679	2.4116
	G-Ste2	3.3800	0.7940	4.8000	1.0518	1.9136	3.3566	−12.4222	0.2846	0.0001	−0.9761	7.0567
	G-Ste3	4.0200	0.6000	5.2000	0.7338	1.8411	3.9012	−5.4129	0.7074	−0.0002	0.5008	5.0634
	G-Ste4	5.3600	0.8530	6.5000	1.4309	0.9725	5.3175	−17.3922	0.2424	0.0002	−0.5096	15.2591

the curve, Cosenza et al. (Cosenza et al., 1995) proposed CMR model, which can better express the development trend of bond-slip curve between FRP bars and concrete in the ascending phase. The expression of the CMR model is shown in Eq. 8:

$$\frac{\tau}{\tau_{max}} = \left(1 - \exp\left(-\frac{s}{s_r}\right)\right)^{\beta} \quad (0 \leqslant s \leqslant s_{max}) \tag{8}$$

where τ and s are bond stress and slip, respectively. τ_{max} is the maximum bond stress under the ultimate load. S_r and β are parameters that require curve fitting from the test data.

3.4.3.2 2P model

In part of the bond-slip curve obtained by the mBPE model, the descending section shows a linear trend, while the CMR model only shows the rising section on the bond-slip curve. Therefore, Wei (Wei et al., 2019) proposed the 2P model based on bonding mechanism and bonding characteristics, which can better represent the accuracy of the bond-slip constitutive model. The expression of the 2P model is shown in Eq. 9:

$$\tau = be^{-\eta s}\cos(\omega s + \varphi) + c \tag{9}$$

where τ and s are bond stress and slip, respectively. b、η、ω、φ、c are parameters that require curve fitting from the test data.

3.4.3.3 Comparisons between the mBPE, CMR models and 2P models

In this paper, mBPE model, CMR model and 2P model (the relevant parameters of the model are shown in Table 5) are used to establish bond-slip curves. Root mean squared error (RMSE) is used to compare the mBPE, CMR and 2P models, to obtain the applicability and accuracy of the models. The calculation formula of RMSE is shown in Eq. 10, and the calculation results are shown in Table 6. The results show that the fitting effect of mBPE model and 2P model is the best, and the fitting effect is more accurate in the upstream section than that of mBPE model and CMR model.

$$RMSE = \sqrt{\frac{\sum\left(\tau_{exp} - \tau_{fit}\right)^2}{n}} \tag{10}$$

where τ_{exp} is test value of bond stress. τ_{fit} is the fitting value of bond stress. n is the number of test data.

Figures 10–13 are the bond-slip curves of test beams under different models. The figure shows that the bond-slip curves between mBPE, CMR and 2P models have similar trends, but the mBPE model and 2P model have better correlation. On the other hand, the RMSE of the mBPE model and the 2P model are smaller than that of the CMR model, indicating that the mBPE model and the 2P model are more in line with the actual bond slip trend of GFRP reinforcement.

4 Correlation model analysis of pore structure and bonding performance of steam-cured concrete

There are many factors that influence the bonding performance, such as the GFRP bar diameter, anchor length, and concrete compressive strength (Yoo and Yoon, 2017; Xingyu et al., 2020). In

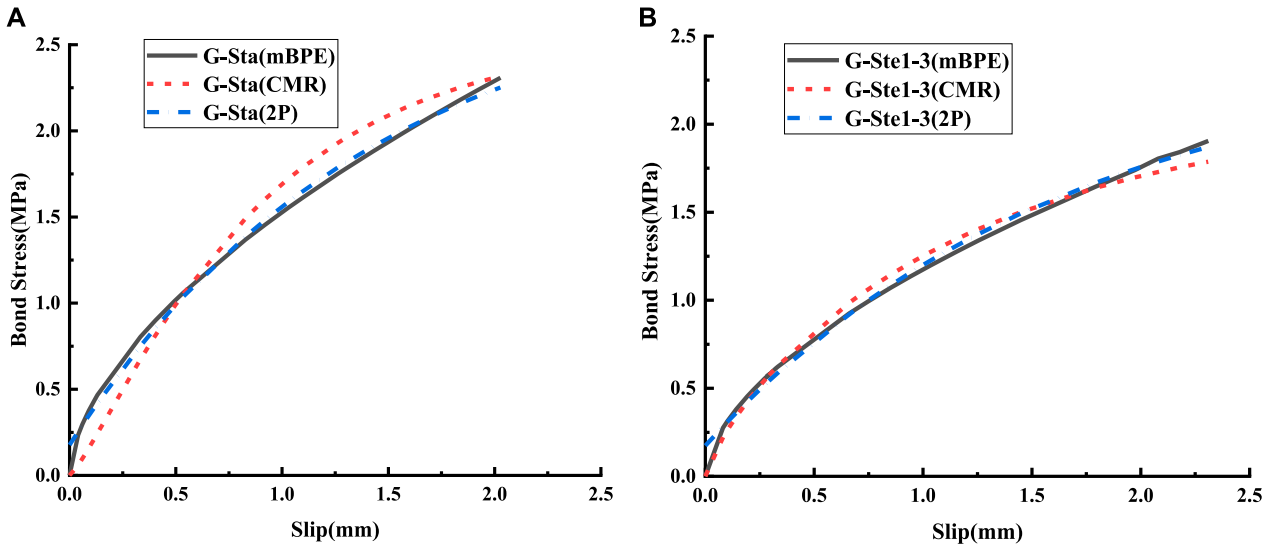

FIGURE 10
Bond-slip curves under different curing methods: **(A)** Bond slip curve under standard curing; **(B)** Bond slip curve under steam curing.

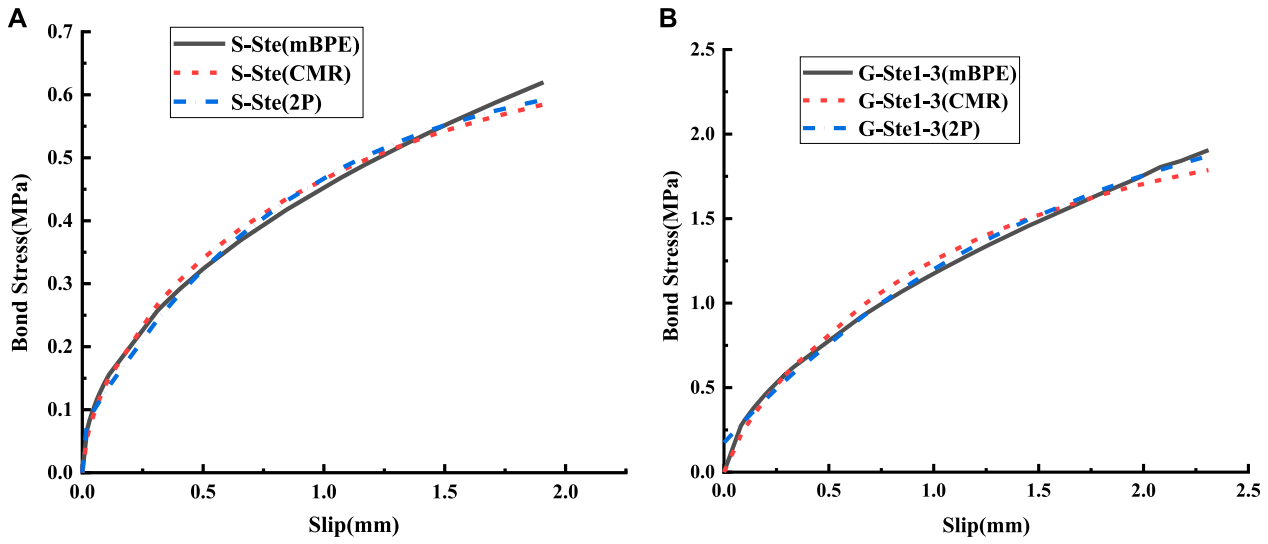

FIGURE 11
Bond-slip curves of different steels: **(A)** Bond slip curve of reinforced concrete beams; **(B)** Bond slip curve of GFRP reinforced concrete beams.

the correlation model analysis, the influence of the porosity of steam-cured concrete was considered in addition to the diameter, anchoring length, and compressive strength of concrete.

Zheng and Xue (Zheng and Xue, 2008) considered the influence of the bonding length and the diameter of the GFRP bars on the bonding strength by introducing the bonding length coefficient (ϕ), defined as follows:

$$\frac{\tau_u}{(8.00 - 0.17d_b)f_t} = k\phi\left(\frac{l_e}{d_b}\right)^{-0.4} \tag{11}$$

In this formula, k is an undetermined coefficient. When $l_e \leq 10d_b$, $\phi = 2.05$, when $l_e = 20d_b$, $\phi = 1.05$, and when $10d_b < l_e < 20d_b$, ϕ is a linear interpolation.

As shown in Table 7, the bond strength of steam-cured concrete and GFRP rods increased gradually with increasing diameter for G-Ste1-3, G-Ste2, G-Ste3 and G-Ste4. This indicates that this is not only related to the ratio of anchor length to diameter, but also to the damage caused by steam maintenance due to the increase in diameter. It can be seen from the change of bond strength in the three models that the bond strength of G-Ste2, G-Ste3 and G-Ste4 increases with the

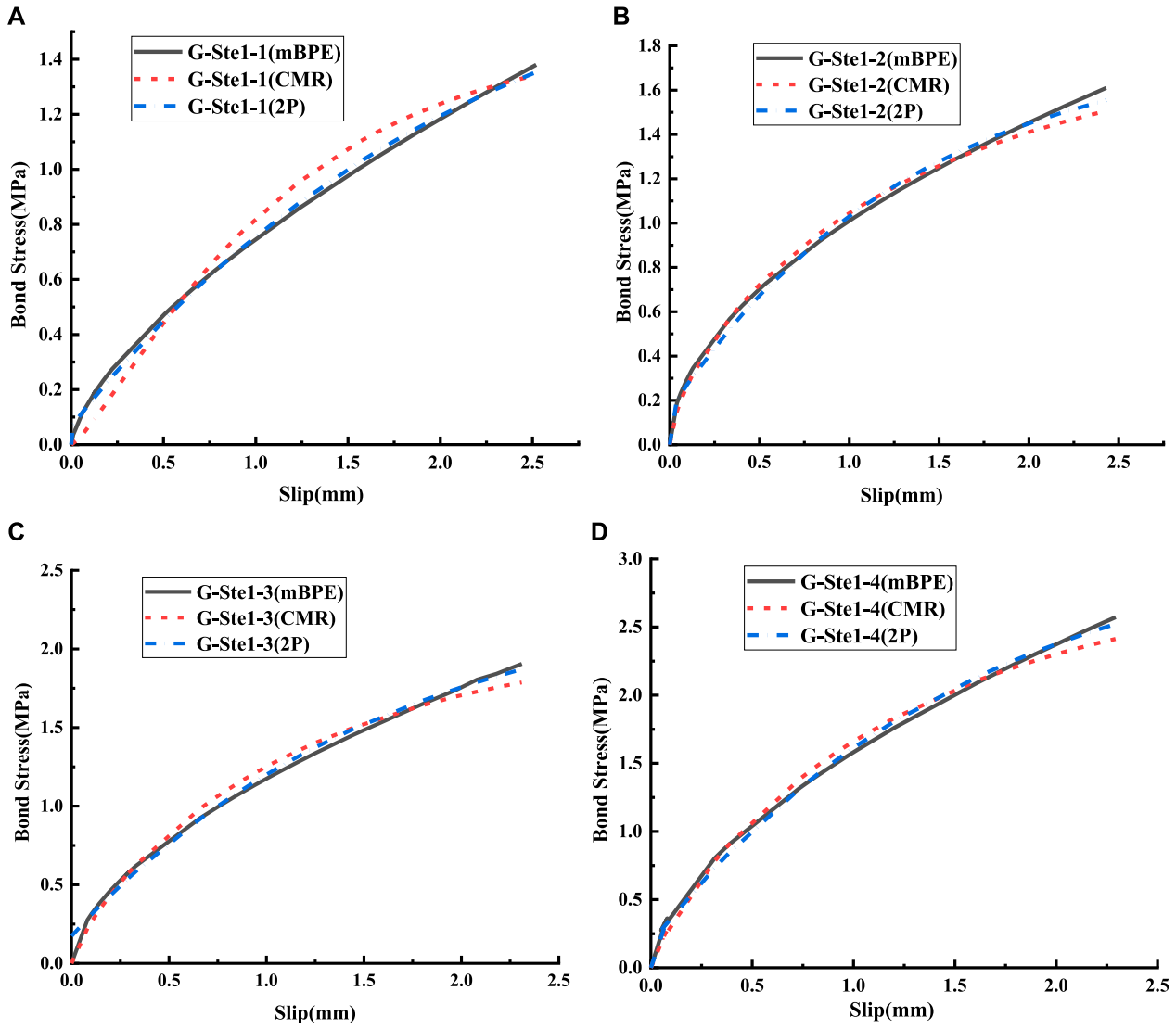

FIGURE 12
Bond-slip curves of different concrete cover thickness: **(A)** The thickness of the concrete protective layer is 15 mm; **(B)** The thickness of the concrete protective layer is 20 mm; **(C)** The thickness of the concrete protective layer is 25 mm; **(D)** The thickness of the concrete protective layer is 35 mm.

increase of bond length. The change of bonding strength is shown in Figure 14.

(1) Coefficient of bond length influence

The differences of the tensile properties between the steam-cured and standard-cured concrete affected the bonding performances of the steam-cured concrete and GFRP bars. Therefore, the following model was used to comprehensively consider the influence of the concrete tensile strength and l_e/d_b:

$$Y_d = \frac{\tau_u}{(8.00 - 0.17d_b)f_t} = K_d\left(\frac{l_e}{d_b}\right)^t \tag{12}$$

where K_d *and* t are the fitting parameters.

The fitting of the test data is shown in Figure 15, and the fitting formula is shown in Eq. 13 According to the RMSE value, the fitting effect between different models is evaluated. The RMSE value of mBPE model is 0.02 and closest to the test value. Therefore, when the variable is the bond length, the mBPE model is finally selected to establish the pore characteristic damage study.

$$\frac{\tau_u}{(8.00 - 0.17d_b)f_t} = \begin{cases} 51.86\left(\frac{l_e}{d_b}\right)^{-1.99} & mBPE \\ 43.21\left(\frac{l_e}{d_b}\right)^{-1.82} & CMR \\ 55.03\left(\frac{l_e}{d_b}\right)^{-2.02} & 2P \\ 47.71\left(\frac{l_e}{d_b}\right)^{-1.92} & exp \end{cases} \tag{13}$$

(2) Coefficient of porosity influence

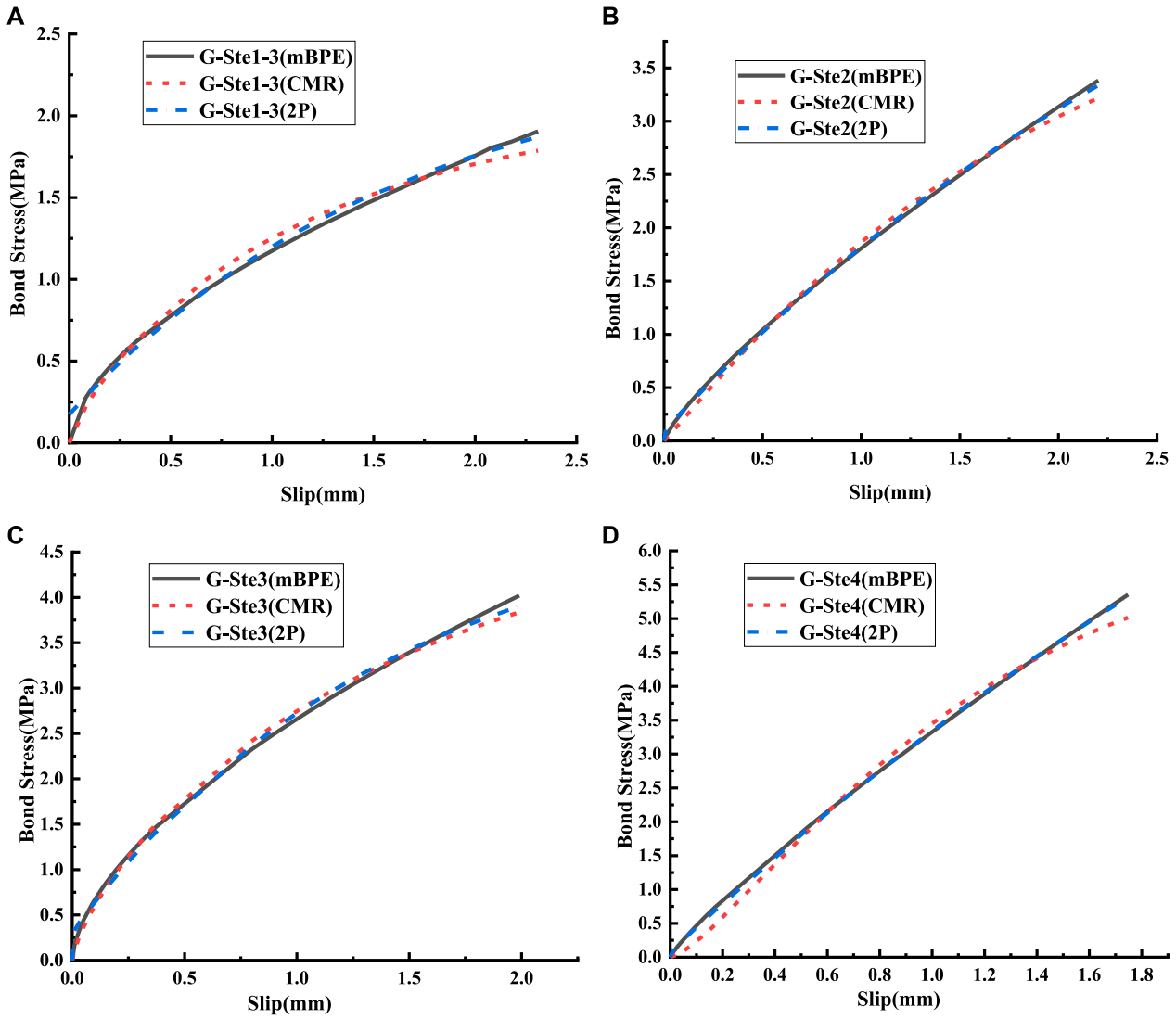

FIGURE 13
Bond-slip curves of different GFRP bar diameters: **(A)** Composite reinforcement with a diameter of 10 mm; **(B)** Composite reinforcement with a diameter of 16 mm; **(C)** Composite reinforcement with a diameter of 19 mm; **(D)** Composite reinforcement with a diameter of 22 mm.

The concrete porosity will directly affect the bonding area and reduce the bond performance. Table 4; Table 7 show that the porosity varied with the thickness of the concrete cover, resulting in different bonding strengths. There was a linear variation trend between the two, which agreed with the variation trend of the bond strength calculation method and the thickness of the concrete cover according to *ACI 440.1R-15* (ACI Committee 440, 2015). It can be seen from the change of bond strength in the three models that the bond strength of G-Ste1-1/2/3/4 increases with the increase of porosity. The change of bonding strength is shown in Figure 16. The bond strength model is shown in Eq. 14:

$$Y_p = \frac{\tau_u}{(8.00 - 0.17d_b)f_t} = K_p + wp \tag{14}$$

Where K_c and w are the test fitting parameters.

The fitting formula is shown in Eq. 15 and the RMSE value is used to evaluate the fitting effect between different models. Therefore, when the variable is porosity, the 2P model is selected to establish the pore-characteristic damage study.

The fit of the test data is shown in Figure 17. The bonding strengths of the steam-cured concrete and the GFRP bars with different porosities were determined.

$$\frac{\tau_u}{(8.00 - 0.17d_b)f_t} = \begin{cases} 0.52 - 0.03P\ mBPE \\ 0.48 - 0.03P\ CMR \\ 0.52 - 0.03P\ 2P \\ 0.51 - 0.03P\ exp \end{cases} \tag{15}$$

The above analysis model was mainly based on the test results, and it was used to perform data fitting. When considering the effects of the maintenance mode, diameter, and concrete cover thickness on

10.3389/fmats.2023.1190031

TABLE 7 Parameters related to maximum bond strength.

Contrast	Specimen number	Tensile strength of concrete axis	Diameter	Thickness of concrete cover	Anchoring section	Anchor length/diameter	Porosity	Maximum bond strength		
		f_t :(MPa)	d_b :(mm)	C: (mm)	l_e :(mm)	$\frac{l_e}{d_b}$	P: (%)	τ_{max} :(MPa)		
								mBPE	CMR	2P
Different forms of maintenance	G-Sta	3.1	10	25	250	25	6.7	2.30	2.56	2.25
	G-Ste1-3	2.9	10	25	250	25	12.9	1.90	2.10	1.87
Different concrete cover thickness	G-Ste1-1	2.9	10	15	250	25	13.9	1.40	1.50	1.35
	G-Ste1-2	2.9	10	20	250	25	13.5	1.60	1.85	1.55
	G-Ste1-3	2.9	10	25	250	25	13	1.90	2.10	1.87
	G-Ste1-4	2.9	10	35	250	25	11.9	2.60	2.90	2.52
Different diameters	G-Ste1-3	2.9	10	25	250	25	13	1.90	2.10	1.87
	G-Ste2	2.9	16	25	250	15.6	13	3.40	4.80	3.34
	G-Ste3	2.9	19	25	250	13.2	13	4.00	5.20	3.90
	G-Ste4	2.9	22	25	250	11.4	13	5.40	6.50	5.32

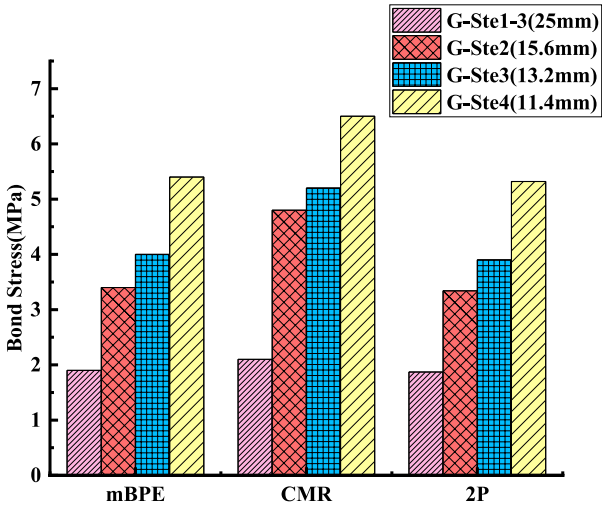

FIGURE 14
Relationship between bond strength and bond length under different models.

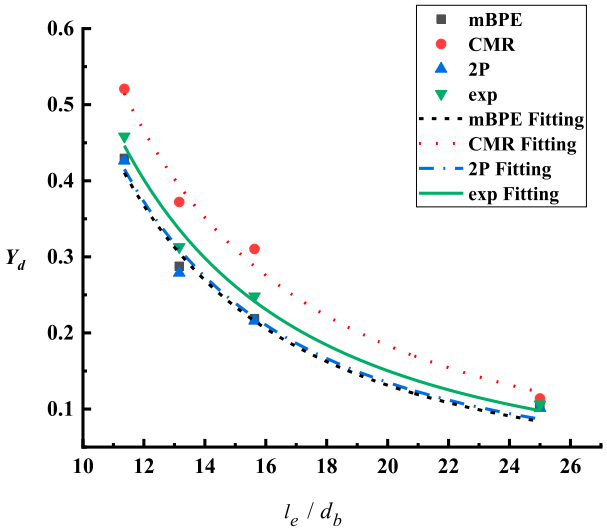

FIGURE 15
Variation of maximum bond strength with l_e/d_b ratio.

the bond strength model, the base number for each working condition needs to be integrated, and the final model for the data integration accounts for the effect of the concrete tensile strength f_t as follows:

$$\frac{\tau_u}{(8.00 - 0.17d_b)f_t} = \alpha + \beta p + \gamma\left(\frac{l_e}{d_b}\right)^x \tag{16}$$

where α, β, γ, and x were all obtained by fitting during the experiment. The bond strength model of the steam-cured concrete and the GFRP bars is expressed by Equation 14. Figure 18 shows that the fitted model was reliable based on comparative analysis of the fitted bond strength model and the test values.

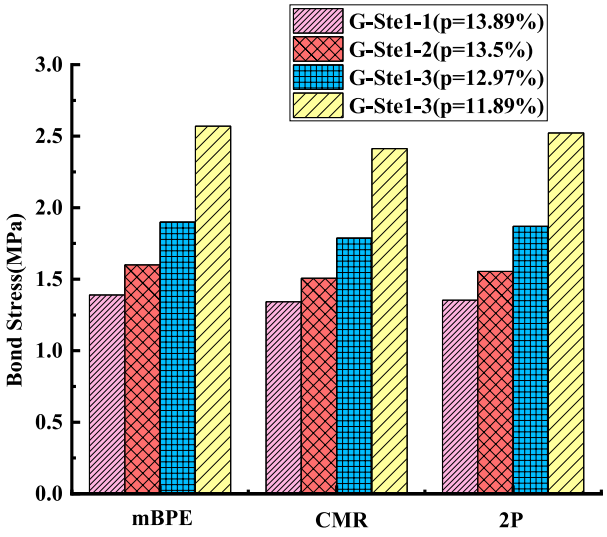

FIGURE 16
Relationship between bond strength and porosity under different models.

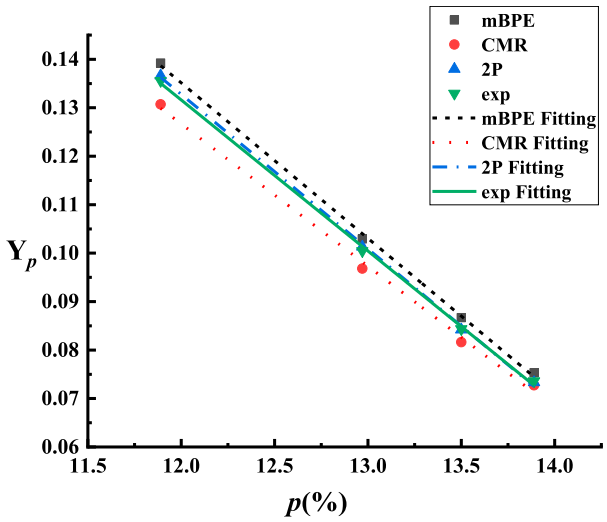

FIGURE 17
Variation of maximum bond strength with l_e/d_b ratio.

$$\frac{\tau_u}{(8.00-0.17d_b)f_t} = 0.44 + 0.03p + 41.5\left(\frac{l_e}{d_b}\right)^{-1.99} \quad (17)$$

5 Discussion

The tensile strength damage and bonding performance damage of GFRP bars in steam cured concrete are significantly lower than those of steel bars. Moreover, due to the increase in harmful pore structures in steam cured concrete, the difference in corrosion degree between steel bars and GFRP bars will be greater during long-term service. Steam cured

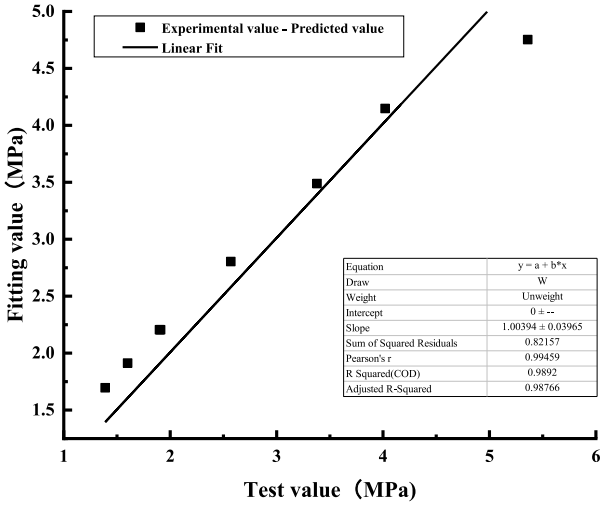

FIGURE 18
Comparative analysis of fitted value and test value.

reinforced concrete prefabricated components face greater durability issues. Therefore, replacing or partially replacing steel bars with high-strength and corrosion-resistant GFRP bars in steam cured concrete prefabricated components is indeed an effective way to solve the low service life of steam cured concrete prefabricated components. However, steam curing has caused damage to the later strength, capillary water absorption performance, and pore structure of concrete, which can have a certain impact on the bonding performance of GFRP bars in concrete. In addition to the high-temperature and high humidity environment of steam curing, the structural performance changes of steam cured concrete and the surface damage of GFRP bars are the main reasons for the bond strength damage of both. Studying any aspect of damage alone is not enough for the overall structure. Based on the classic bond slip constitutive model, using existing specifications and some researchers' research to calculate bond strength models, a bond strength damage prediction model for steam cured concrete and GFRP reinforcement was established. The model fully considers factors such as diameter, anchorage length, protective layer thickness, and concrete strength.

6 Conclusion

Analysis of the microscopic and macroscopic experimental results showed that the distribution of the concrete pore structure changed during steam curing at high temperatures and humidity, affecting the bonding of concrete and GFRP bars.

(1) Significant peeling and micro-cracking occurred on the surface of the steam-cured concrete. However, the interface comparison after cutting and polishing showed that the internal composition of the steam-cured concrete was no different from that of standard-cured concrete. Based on the analysis of the microstructure of the steam-cured concrete, the hydration products were not changed, but the density of the hydration products changed during the steam curing at high temperatures and humidity.

(2) The porosity of the steam-cured concrete was higher than that of the standard-cured concrete, and the solid-to-pore ratio was lower. The number of gel pores smaller than 20 nm accounted for 12.27% of the total number of pores on average, which was about twice the proportion of the gel pores of this size in the standard-cured concrete. The proportion of less harmful pores in the steam-cured concrete was lower than that of the standard-cured concrete. In contrast, the proportion of harmful pores and multi-harmful pores in the total pore size was significantly higher than that in standard-cured concrete. This showed that the distribution of the pore structure in the steam-cured concrete was significantly affected by the steam curing at high temperatures and humidity.

(3) The bond strength of the steam-cured concrete and GFRP bars was 30% lower than that of standard-cured concrete. The bond strength varied with the thickness of the concrete cover and the diameter. The maximum bond strength of the steam-cured concrete and the GFRP bars increased with the increase in the concrete cover thickness and diameter.

(4) Based on the classical bond-slip constitutive model, the damage prediction model of bond strength between steam cured concrete and GFRP bar is established by using existing specifications and some researchers. The model takes into account the effects of porosity, diameter, anchorage length and concrete strength on bond-slip strength. The results show that the fitting value is close to the test value, and the fitting effect is better.

(5) Based on the results of damage test research, a damage prediction model was established for the strength (compressive and tensile) of steam cured concrete, the tensile strength of GFRP bars in steam cured concrete, and the bonding strength between the two.

Data availability statement

The original contributions presented in the study are included in the article/Supplementary Material, further inquiries can be directed to the corresponding author.

Author contributions

ZT: Data curation, Writing—Original draft. WY: Methodology, Supervision, Conceptualization. KZ: Supervision. WW: Supervision, Writing—Reviewing and Editing. WQ: Experiment participation. SW: Experiment participation. All authors contributed to the article and approved the submitted version.

Funding

This study was funded by the Natural Science Foundation of Jiangxi Province (grant number 20181BAB216027), the Science and Technology Project Founded by the Education Department of Jiangxi Province (grant number GJJ170486), the Key Science and Technology Project of Jiangxi Provincial Department of Transportation (Project No. 2016C0007) and the Research Fund for the Doctoral Program of Higher Education of China (grant number DHBK2017119).

Conflict of interest

The authors declare that the research was conducted in the absence of any commercial or financial relationships that could be construed as a potential conflict of interest.

Publisher's note

All claims expressed in this article are solely those of the authors and do not necessarily represent those of their affiliated organizations, or those of the publisher, the editors and the reviewers. Any product that may be evaluated in this article, or claim that may be made by its manufacturer, is not guaranteed or endorsed by the publisher.

References

ACI (American Concrete Institute) (2005). *Guide for the design and construction of concrete reinforced with FRP bars*. Farmington Hills, MI: ACI Publishing.

ACI (American Concrete Institute) (2006). *Guide for the design and construction of structural concrete reinforced with FRP bars*. Farmington Hills, MI: ACI Publishing. ACI 440.1 R-06.

ACI Committee 440 (2015). *Guide for the design and construction of structural concrete reinforced with fiber reinforced polymer bars"*. Farmington Hills, MI: ACI Publishing. ACI 440.1R-15.

Al-Sibahy, A., and Sabhan, M. (2020). Corrosion effects on the bond behaviour of steel bars in self-compacting concrete. *Constr. Build. Mater.* 250, 118568. doi:10.1016/j.conbuildmat.2020.118568

Altalmas, A., El Refai, A., and Abed, F. (2015). Bond degradation of basalt fiber-reinforced polymer (BFRP) bars exposed to accelerated aging conditions. *Constr. Build. Mater.* 81, 162–171. doi:10.1016/j.conbuildmat.2015.02.036

Bakis, C. E., Boothby, T. E., and Jia, J. (2007). Bond durability of glass fiber-reinforced polymer bars embedded in concrete beams. *J. Compos. Constr.* 11 (3), 269–278. doi:10.1061/(asce)1090-0268(2007)11:3(269)

Bi, L., Long, G., Ma, C., and Xie, Y. (2021). Experimental investigation on the influence of phase change materials on properties and pore structure of steam-cured mortar. *Archives Civ. Mech. Eng.* 21 (1), 11–10. doi:10.1007/s43452-020-00170-7

Chen, L., Zheng, K., Xia, T., and Long, G. (2019). Mechanical property, sorptivity and microstructure of steam-cured concrete incorporated with the combination of metakaolin-limestone. *Case Stud. Constr. Mater.* 11, e00267. doi:10.1016/j.cscm.2019.e00267

Cieszko, M., Kempiński, M., and Czerwiński, T. (2019). Limit models of pore space structure of porous materials for determination of limit pore size distributions based on mercury intrusion data. *Transp. Porous Media* 127 (2), 433–458. doi:10.1007/s11242-018-1200-5

Cosenza, E., Manfredi, G., and Realfonzo, R. (1995). Analytical modelling of bond between FRP reinforcing bars and concrete, Proceedings of the non-metallic (FRP) reinforcement for concrete structures" - proceedings of the second international RILEM symposium(FRPRCS-2).Ghent, Belgium, January 1995

Ellis, D. S., Tabatabai, H., and Nabizadeh, A. (2018). Residual tensile strength and bond properties of GFRP bars after exposure to elevated temperatures. *Mater.* 11 (3), 346. doi:10.3390/ma11030346

Esfahani, M. R., Rakhshanimehr, M., and Mousavi, S. R. (2013). Bond strength of lap-spliced GFRP bars in concrete beams. *J. Compos. Constr.* 17 (3), 314–323. doi:10.1061/(ASCE)CC.1943-5614.0000359

Esmaeili, Y., Eslami, A., Newhook, J., and Benmokrane, B. (2020). Performance of GFRP-reinforced concrete beams subjected to high-sustained load and natural aging for 10 years. *J. Compos. Constr.* 24 (5), 04020054. doi:10.1061/(ASCE)CC.1943-5614.0001065

Focacci, F., Nanni, A., and Bakis, C. E. Local bond-slip relationship for FRP reinforcement in concrete. *J. Compos. Constr.*, 2000, 4(1): 24–31. doi:10.1061/(asce)1090-0268(2000)4:1(24)

Han, F., Song, S., Liu, J., and Huang, S. (2019). Properties of steam-cured precast concrete containing iron tailing powder. *Powder Technol.* 345, 292–299. doi:10.1016/j.powtec.2019.01.007

Hong, S., Kim, S., Lee, Y., and Jeong, J. (2018). Estimation of compressive strength of reinforced concrete structure using impact testing method and rebound hardness method. *Archit. Res.* 20 (4), 137–145. doi:10.5659/AIKAR.2018.20.4.137

Isleem, H. F., Tayeh, B. A., Alaloul, W. S., Musarat, M. A., and Raza, A. (2021). Artificial neural network (ANN) and finite element (FEM) models for GFRP-reinforced concrete columns under axial compression. *Mater.* 14 (23), 7172. doi:10.3390/ma14237172

Jiang, P., Jiang, L., Zha, J., and Song, Z. (2017). Influence of temperature history on chloride diffusion in high volume fly ash concrete. *Constr. Build. Mater.* 144, 677–685. doi:10.1016/j.conbuildmat.2017.03.225

Liu, B., Jiang, J., Shen, S., Zhou, F., Shi, J., and He, Z. (2020b). Effects of curing methods of concrete after steam curing on mechanical strength and permeability. *Constr. Build. Mater.* 256, 119441. doi:10.1016/j.conbuildmat.2020.119441

Liu, B., Shi, J., Zhou, F., Shen, S., Ding, Y., and Qin, J. (2020a). Effects of steam curing regimes on the capillary water absorption of concrete: Prediction using multivariable regression models. *Constr. Build. Mater.* 256, 119426. doi:10.1016/j.conbuildmat.2020.119426

Liu, M., Tan, H., and He, X. (2019). Effects of nano-SiO2 on early strength and microstructure of steam-cured high volume fly ash cement system. *Constr. Build. Mater.* 194, 350–359. doi:10.1016/j.conbuildmat.2018.10.214

Lü, Q., Qiu, Q., Zheng, J., Wang, J., and Zeng, Q. (2019). Fractal dimension of concrete incorporating silica fume and its correlations to pore structure, strength and permeability. *Constr. Build. Mater.* 228, 116986. doi:10.1016/j.conbuildmat.2019.116986

Maranan, G., Manalo, A., Karunasena, K., and Benmokrane, B. (2015). Bond stress-slip behavior: Case of GFRP bars in geopolymer concrete. *J. Mater. Civ. Eng.* 27 (1), 04014116. doi:10.1061/(ASCE)MT.1943-5533.0001046

Maruyama, T., Karasawa, H., and Date, S. (2017). Effect of type of cement and expansive agent on the hardening of steam-cured concrete. *Trans. Tech. Publ. Ltd.* 744, 105–113. doi:10.4028/www.scientific.net/KEM.744.105

Press, W. H., Teukolsky, S. A., and Vetterling, W. T. (2007). "Numerical recipes," in *The art of scientific computing*. 3rd edition (Cambridge: Cambridge University Press).

Rossi, C. R. C., C Oliveira, D. R., Picanço, M. S., Pompeu Neto, B. B., and Oliveira, A. M. (2020). Development length and bond behavior of steel bars in steel fiber–reinforced concrete in flexural test. *J. Mater. Civ. Eng.* 32 (1), 04019333. doi:10.1061/(ASCE)MT.1943-5533.0002979

Shi, J., Liu, B., Wu, X., Tan, J., Dai, J., and Ji, R. (2020a). Effect of steam curing on surface permeability of concrete: Multiple transmission media. *J. Build. Eng.* 32, 101475. doi:10.1016/j.jobe.2020.101475

Shi, J., Liu, B., Zhou, F., Shen, S., Dai, J., Ji, R., et al. (2020b). Heat damage of concrete surfaces under steam curing and improvement measures. *Constr. Build. Mater.* 252, 119104. doi:10.1016/j.conbuildmat.2020.119104

Shi, J., Liu, B., Zhou, F., Shen, S., Guo, A., and Xie, Y. (2021). Effect of steam curing regimes on temperature and humidity gradient, permeability and microstructure of concrete. *Constr. Build. Mater.* 281, 122562. doi:10.1016/j.conbuildmat.2021.122562

Sidiq, A., Gravina, R. J., Setunge, S., and Giustozzi, F. (2020). High-efficiency techniques and micro-structural parameters to evaluate concrete self-healing using X-ray tomography and mercury intrusion porosimetry: A review. *Constr. Build. Mater.* 252, 119030. doi:10.1016/j.conbuildmat.2020.119030

Sidiq, A., Gravina, R. J., Setunge, S., and Giustozzi, F. (2019). Microstructural analysis of healing efficiency in highly durable concrete. *Constr. Build. Mater.* 215, 969–983. doi:10.1016/j.conbuildmat.2019.04.233

Troian-Gautier, L., Beauvilliers, E. E., Swords, W. B., and Meyer, G. J. (2016). Redox active ion-paired excited states undergo dynamic electron transfer. *J. Am. Chem. Soc.* 138 (51), 16815–16826. doi:10.1021/jacs.6b11337

Wang, J., Long, G., Xiang, Y., Dong, R., Tang, Z., Xiao, Q., et al. (2022). Influence of rapid curing methods on concrete microstructure and properties: A review. *Case Stud. Constr. Mater.* 17, e01600. doi:10.1016/j.cscm.2022.e01600

Wang, L., Mao, Y., Lv, H., Chen, S., and Li, W. (2018). Bond properties between FRP bars and coral concrete under seawater conditions at 30, 60, and 80 °C. *Constr. Build. Mater.* 162, 442–449. doi:10.1016/j.conbuildmat.2017.12.058

Wang, M., Xie, Y., Long, G., Ma, C., Zeng, X., and Qiang, F. (2020). The impact mechanical characteristics of steam-cured concrete under different curing temperature conditions. *Constr. Build. Mater.* 241, 118042. doi:10.1016/j.conbuildmat.2020.118042

Wang, Y. L. (2013). *Experimental study on tensile properties of FRP bars and the bond properties to concrete after high temperature*. Zhengzhou, China: Zhengzhou University.

Wei, W., Liu, F., Xiong, Z., Lu, Z., and Li, L. (2019). Bond performance between fibre-reinforced polymer bars and concrete under pull-out tests. *Constr. Build. Mater.* 227, 116803. doi:10.1016/j.conbuildmat.2019.116803

Wikidata (2005). *TZ 210-2005, "technical specification for construction of railway concrete works"*. Beijing , China: China Railway Publishing House.

Wu, L., Xu, X., Wang, H., and Yang, J. Q. (2022). Experimental study on bond properties between GFRP bars and self-compacting concrete. *Constr. Build. Mater.* 320, 126186. doi:10.1016/j.conbuildmat.2021.126186

Xingyu, G., Yiqing, D., and Jiwang, J. (2020). Flexural behavior investigation of steel-GFRP hybrid-reinforced concrete beams based on experimental and numerical methods. *Eng. Struct.* 206, 110117. doi:10.1016/j.engstruct.2019.110117

Xu, J., Marsac, R., Costa, D., Cheng, W., Wu, F., Boily, J. F., et al. (2017). Co-Binding of pharmaceutical compounds at mineral surfaces: Molecular investigations of dimer formation at goethite/water interfaces. *Environ. Sci. Technol.* 51 (15), 8343–8349. doi:10.1021/acs.est.7b02835

Yan, F., and Lin, Z. (2017). Bond durability assessment and long-term degradation prediction for GFRP bars to fiber-reinforced concrete under saline solutions. *Compos. Struct.* 161, 393–406. doi:10.1016/j.compstruct.2016.11.055

Yang, W. (2016). *Damage research on steam-curing GFRP reinforced precast concrete components in high-speed railway*. Hubei, China: Wuhan University of Technology.

Yang, W., He, X., Zhang, K., Yang, Y., and Dai, L. (2017). Combined effects of curing temperatures and alkaline concrete on tensile properties of GFRP bars. *Int. J. Polym. Sci.* 2017, 1–8. doi:10.1155/2017/4262703

Yang, W., Tang, Z., Wu, W., Zhang, K., Yuan, J., and Li, H. (2022). Effect of different fibers on impermeability of steam cured recycled concrete. *Constr. Build. Mater.* 328, 127063. doi:10.1016/j.conbuildmat.2022.127063

Yoo, D. Y., Kwon, K. Y., Park, J. J., and Yoon, Y. S. (2015). Local bond-slip response of GFRP rebar in ultra-high-performance fiber-reinforced concrete. *Compos. Struct.* 120, 53–64. doi:10.1016/j.compstruct.2014.09.055

Yoo, D. Y., and Yoon, Y. S. (2017). Bond behavior of GFRP and steel bars in ultra-high-performance fiber-reinforced concrete. *Adv. Compos. Mater.* 26 (6), 493–510. doi:10.1080/09243046.2016.1197493

Zeyad, A. M., Johari, M. A. M., Abutaleb, A., and Tayeh, B. A. (2021). The effect of steam curing regimes on the chloride resistance and pore size of high–strength green concrete. *Constr. Build. Mater.* 280, 122409. doi:10.1016/j.conbuildmat.2021.122409

Zhang, K., Yang, W., Li, H., Tang, Z., Wu, W., Yuan, J., et al. (2021). Semi-reliability probability damage assessment of GFRP bars embedded in steam-curing concrete beams based on the multiple factors related moisture absorption model. *Polymers* 13 (24), 4409. doi:10.3390/polym13244409

Zheng, J. J., Dai, J. G., and Fan, X. L. (2016). Fracture analysis of frp-plated notched concrete beams subjected to three-point bending. *J. Eng. Mech.* 142 (3), 04015096. doi:10.1061/(ASCE)EM.1943-7889.0001021

Zheng, Q. W., and Xue, W. -C. (2008). Bond slip constitutive relation of GFRP bars with sand deformation. *Eng. Mech.* (09), 162–169.

Zhou, X., Zhao, H., Xie, Y., Long, G., Zeng, X., Li, J., et al. (2022). Mechanical behavior of bonded interface between steam-cured concrete and SCC under direct shear test: Experimental and numerical studies. *J. Build. Eng.* 63, 105517. doi:10.1016/j.jobe.2022.105517

Zou, C., Long, G., Xie, Y., He, J., Ma, C., and Zeng, X. (2019). Evolution of multi-scale pore structure of concrete during steam-curing process. *Microporous Mesoporous Mater.* 288, 109566. doi:10.1016/j.micromeso.2019.109566

Zou, C., Long, G., Zeng, X., Ma, K., and Xie, Y. (2021). Hydration and multiscale pore structure characterization of steam-cured cement paste investigated by X-ray CT. *Constr. Build. Mater.* 282, 122629. doi:10.1016/j.conbuildmat.2021.122629

10.3389/fmats.2023.1190031

Nomenclature

A_f	The cross-sectional area
A_b	Section area of reinforcement
b	The width of beams
C	Slip parameter
c	Concrete cover thickness
d	Diameter
d_b	Diameter of reinforcement
E	Elasticity Modulus
E_b	Elasticity modulus of reinforcement
E_f	Longitudinal modulus of elasticity
F	Ultimate tension
f_t	Tensile strength of concrete axis
h	Height
K_c	Fitting parameters
K_d	Fitting parameters
K_T	Reduction factor
k	Undetermined coefficient
l	Length
l_e	Anchoring section
N_{smax}	Maximum slip load
P	Load
p	Porosity
R	Tensile Strength
S	Slip value
S_c	Corresponding slip value τ_c
S_{max}	Corresponding slip value τ_{max}
t	Fitting parameters
w	Fitting parameters
x	Fitting parameters
α	Fitting parameters
β	Fitting parameters
γ	Fitting parameters
τ	Bond strength
τ_c	Corresponding bond strength at the beginning of linear slip
τ_{max}	Maximum bond strength
ϕ	Linear interpolation
ρ	Fitting parameters
b	Fitting parameters
η	Fitting parameters
ω	Fitting parameters
φ	Fitting parameters
Y_d	Calculated value of bond strength
Y_p	Calculated value of bond strength